



1 **Soil organic carbon distribution for 0-3 m soils at 1 km²**
2 **scale of the frozen ground in the Third Pole Regions**

3

4 Dong Wang^{1,2}, Tonghua Wu^{1,3*}, Xiaodong Wu¹, Xianhua Wei⁴, Cuicui Mu⁵, Ren Li¹, Guojie
5 Hu¹, Defu Zou¹, Xiaofan Zhu¹, Jie Chen¹, Junmin Hao⁶, Jie Ni^{1,2}, Xiangfei Li^{1,2}, Wensi
6 Ma^{1,2}, Amin Wen^{1,2}, Chenpeng Shang^{1,2}, Yune La^{1,2}, Xin Ma^{1,2}

7

8 ¹ Cryosphere Research Station on the Qinghai-Tibetan Plateau, State Key Laboratory of
9 Cryospheric Science, Northwest Institute of Eco-Environment and Resource, Chinese
10 Academy of Sciences, Lanzhou, Gansu 730000, China

11 ² University of Chinese Academy Sciences, Beijing, 100049, China.

12 ³ Southern Marine Science and Engineering Guangdong Laboratory, Guangzhou 511458,
13 China.

14 ⁴ College of geography and environmental science, Northwest Normal University, Lanzhou
15 730070, China.

16 ⁵ Key Laboratory of Western China's Environmental Systems (Ministry of Education),
17 College of Earth and Environmental Sciences, Lanzhou University, Lanzhou, 730000,
18 China.

19 ⁶ School of civil engineering, Lanzhou University of Technology, Lanzhou, 730050, China.

20 *Correspondence: Tonghua Wu (thuawu@lzb.ac.cn)



21 **Abstract:** Soil organic carbon (SOC) is very important in the vulnerable ecological
22 environment of the Third Pole; however, data regarding the spatial distribution of SOC
23 are still scarce and uncertain. Based on multiple environmental variables and soil profile
24 data from 458 pits (depth of 0–1 m) and 114 cores (depth of 0–3 m), this study uses a
25 machine-learning approach to evaluate the SOC storage and spatial distribution at a
26 depth interval of 0–3 m in the frozen ground area of the Third Pole region. Our results
27 showed that SOC stocks (SOCS) exhibited a decreasing spatial pattern from the
28 southeast towards the northwest. The estimated SOC storage in the upper 3 m of the
29 soil profile was 46.18 Pg for an area of 3.27×10^6 km², which included 21.69 Pg and
30 24.49 Pg for areas of permafrost and seasonally frozen ground, respectively. The mean
31 SOCS under different vegetation types showed a decreasing pattern as follows: forest >
32 shrub > cropland > grassland > desert. Among all soil orders, histosols and gleisols had
33 the largest SOCSs, while gypsisols and salt flats had the smallest SOCS. Our results
34 provide information on the storage and patterns of SOCS at a 1 km² scale for areas of
35 frozen ground in the Third Pole region, thus providing a scientific basis for future
36 studies pertaining to Earth system models. The dataset is open-access and available at
37 <https://doi.org/10.5281/zenodo.4293454> (Wang et al., 2020).

38 **1 Introduction**

39 Soil is an important part of the global terrestrial ecosystem and represents the
40 largest terrestrial organic carbon pool with the longest turnover time (Amundson, 2001).
41 This is especially true in areas of frozen ground, including permafrost and seasonally
42 frozen ground. In cold environments, soil accumulates substantial organic carbon due
43 to slow decomposition rates and repeated freeze–thaw cycles (Fan et al., 2012; Li et al.,
44 2020). It has been reported that more than half of the world’s soil organic carbon (SOC)
45 is stored in permafrost regions (Hugelius et al., 2014; Ping et al., 2015). Even slight
46 changes in the decomposition of the SOC pool in permafrost regions might lead to
47 significant changes in the atmospheric CO₂ concentration, which plays an important
48 role in regulating and stabilizing the carbon balance of global ecosystems (Schuur et
49 al., 2015). Therefore, it is of great significance to accurately estimate the storage and



50 spatial distribution of SOC in regions of frozen ground in order to study the carbon
51 cycle of this ecosystem as well as global change.

52 As the “roof of the world”, the Third Pole is the area of frozen ground at the highest
53 average altitude in the middle and low latitudes of the Northern Hemisphere, where
54 permafrost and seasonally frozen ground cover areas of $\sim 1.72 \times 10^6$ km² and $\sim 1.55 \times$
55 10^6 km², respectively (Obu et al., 2019). The Third Pole is also one of the most sensitive
56 areas with respect to global climate change, and has a warming rate that is
57 approximately twice the global average (Stocker et al., 2013). In the past few decades,
58 permafrost in the Third Pole region has experienced obvious degradation, which is
59 characterized by an increasing ground temperature, a deepening of the active layer, a
60 shrinking permafrost area, an expanding area of seasonally frozen ground, and the
61 development of thermokarst (Mu et al., 2020; Ran et al., 2017; Turetsky et al., 2019;
62 Wu et al., 2012). Permafrost degradation will not only cause serious geological disasters
63 and affect engineering construction in cold areas, but will also accelerate the
64 decomposition of the huge SOC pool stored in permafrost. Moreover, it will emit a large
65 amount of greenhouse gases into the atmosphere, thus increasing the rate of climate
66 change in the future (Schuur et al., 2015). Therefore, accurate estimates of the SOC
67 storage and spatial distribution in the area of frozen ground in the Third Pole region
68 have become important for Earth system modeling. Such estimates are widely used to
69 study the carbon cycle of this ecosystem and global change (Koven et al., 2011;
70 Lombardozi et al., 2016; McGuire et al., 2018).

71 Early studies were mostly based on data from China’s national soil survey, and
72 were combined with regional vegetation/soil maps to estimate the SOC pool for a
73 certain vegetation type or relatively small area (Wang et al., 2002; Zeng et al., 2004).
74 Up until 2008, the Chinese part of the Qinghai-Tibet Plateau (QTP) was taken as an
75 independent geographical unit to estimate the SOC pool in the upper 100 cm of the soil
76 profile (Tian et al., 2008; Wu et al., 2008). However, these studies did not distinguish
77 between regions of permafrost and seasonally frozen ground. Mu et al. (2015) used data
78 from 11 deep sediment cores and previously published data to estimate the SOC storage
79 of permafrost regions on the QTP, and found this to be 27.9 Pg in the upper 2 m of the



80 soil profile and 132.3 Pg below a depth of 2 m. Zhao et al. (2018) used the data of 200
81 soil profile measurements from permafrost zones on the QTP, and reported a SOC
82 storage of 17.07 Pg for the upper 2 m of the soil profile. Subsequently, Jiang et al. (2019)
83 used the second Chinese soil census data and estimated that the total SOC pool for a
84 depth interval of 0–3 m on the QTP was approximately 73.61 Pg. Although the
85 aforementioned studies improved our understanding of SOC storage in the Third Pole
86 region, their results were quite different due to differences in the SOC data sources,
87 number of sampling sites, and research aims. Furthermore, the large-scale maps of
88 vegetation and soil types used in these studies were associated with large uncertainties
89 because they were created years ago and have a low spatial resolution, thus leading to
90 potentially large errors in the estimated total SOC pools.

91 Recently, considerable progress has been made in digital soil mapping methods.
92 Spatial interpolation, linear regression, and machine learning have been widely used to
93 simulate the spatial distribution of SOC in the permafrost region of the QTP (Ding et
94 al., 2016; Ding et al., 2019; Wang et al., 2020; Yang et al., 2008). These studies have
95 provided new spatial data and improved the prediction accuracy of SOC compared with
96 earlier studies. However, few studies to date have systematically assessed SOC pools
97 across areas of seasonally frozen ground in the Third Pole region, which limits many
98 investigations requiring SOC data for these areas. The average elevation of the
99 seasonally frozen ground in the Third Pole region exceeds 3800 m, and there is a colder
100 environment, longer freezing time, and slower decomposition rate of organic matter in
101 comparison to other regions at the same latitude (Chen and Li, 2008). In addition, the
102 total SOC storage cannot be neglected and requires further study.

103 To evaluate the size and high-resolution spatial patterns of SOC stocks in the Third
104 Pole region, we carried out a large-scale field-sampling plan that covered representative
105 permafrost zones over the region's bioclimatic gradient, including a large unpopulated
106 area with harsh natural conditions. A total of 200 soil pits were excavated, most of
107 which were deeper than 2 m (Zhao et al., 2018). In addition, we collected field-
108 measured SOCS data for the Third Pole region from relevant literature published
109 between 2000 and 2016 (Ding et al., 2016; Song et al., 2016; Xu et al., 2019; Yang et



110 al., 2008). By combining high-resolution remotely sensed data and interpolated
111 meteorological datasets, we simulated the spatial distribution of SOCS in the Third Pole
112 region by three machine learning methods and calculated the SOC storage of specific
113 soil intervals (0–30 cm, 0–50 cm, 0–100 cm, 0–200 cm, and 0–300 cm). The results
114 provide basic data for Earth system modeling, and reference methods for studying the
115 spatial distribution of soil elements under complex terrain.

116 **2 Materials and Methods**

117 **2.1 Study area**

118 The Third Pole is the highest plateau in the world, and is located on the QTP and
119 its surrounding mountains, which include Pamir and Hindu Kush mountain ranges in
120 the west, the Hengduan Mountains in the east, the Kunlun and Qilian mountains in the
121 north, and the Himalayas in the south (Yao et al., 2012). In addition, the Third Pole is
122 the largest high-altitude permafrost zone in the Northern Hemisphere, with a total
123 permafrost area of approximately 1.72×10^6 km², thus representing ~8% of permafrost
124 regions in the Northern Hemisphere (Obu et al., 2019). The average active layer
125 thickness is 2.3 m (Qin et al., 2017). The area of seasonally frozen ground covers an
126 area of approximately 1.55×10^6 km², which is mainly located in the eastern and
127 southern parts of the Third Pole as well as at lower elevations of basins.

128 Affected by high altitude, most areas of the Third Pole are dominated by a
129 mountain plateau climate with strong solar radiation. The mean annual precipitation
130 (MAP) ranges from 50 mm to 2000 mm and falls mainly during the growing season
131 from May to September (Ji et al., 2018). The mean annual temperature (MAT) is < 5 °C,
132 which gradually decreases with elevation, and has an obvious vertical climate zone (Qin
133 et al., 2005). The Third Pole is mainly covered by five types of vegetation: forests,
134 shrubs, grasslands, croplands, and deserts (Hao et al., 2017).

135 **2.2 Data Processing**

136 **2.2.1 Soil organic carbon data**

137 The SOC data used in this study included document data and field-measured data
138 (Table 1). 1) Document data: data pertaining to a soil depth interval of 0–30 cm (n =
139 135) was retrieved from Yang et al. (2010) for the SOC database. Data pertaining to a



140 depth interval of 0–100 cm ($n = 93$) was obtained from Xu et al. (2019). Data pertaining
141 to a depth interval of 0–100 cm ($n = 30$) retrieved from Song et al. (2016). Moreover,
142 additional data for 0–3 m and 0–2 m depth intervals ($n = 113$) were retrieved from Ding
143 et al. (2016).

144 2) Field measured data: a total of 200 soil pits were excavated between 2009 and
145 2013; 72 soil pits were excavated manually in 2009, and 128 soil pits were excavated
146 with hydraulic excavators in 2010 and 2011 (Zhao et al., 2018). For each soil profile,
147 we collected soil samples at depth intervals of 0–10 cm, 10–20 cm, 20–30 cm, 30–50
148 cm, 50–100, and 100–200 cm. The bulk density was measured using a bulk soil sampler
149 (5 cm diameter and 5-cm-high stainless-steel cutting ring). The SOC content was
150 determined using the Walkley-black method after soil samples were pretreated by air
151 drying, grinding, and screening. The analyses were carried out in triplicate using
152 subsamples, and the mean of three values was used as the SOC content. The SOCS was
153 calculated using Eq. (1):

$$154 \quad SOCS = \sum_{i=1}^n T_i \times BD_i \times SOC_i \times \frac{(1 - C_i)}{10} \quad (1)$$

155 where T_i , BD_i , SOC_i , and C_i are soil thickness (cm), dried bulk density ($\text{g} \cdot \text{cm}^{-3}$), SOC
156 content (%) and $> 2\text{mm}$ rock fragment content (%) at layer i .

157 2.2.2 Environmental data

158 The environmental covariates used in this study included a digital elevation model
159 (DEM), remotely sensed data, and spatial interpolation data (Table S1).

160 A DEM at a spatial resolution of $1 \text{ km} \times 1 \text{ km}$ was downloaded from the
161 International Scientific Data Service Platform (<http://datamirror.csdb.cn>). Using the
162 DEM data and SAGA GIS software, we calculated 14 terrain attributes: elevation (H),
163 slope (S), aspect (A), plan curvature (PlanC), profile curvature (ProC), topographic
164 wetness index (TWI), total catchment area (TCA), relative slope position (RSP), slope
165 length and steepness factor (LS), convergence index (CI), channel network base level
166 (CNB), channel network distance (CND), valley depth (VD), and closed depressions
167 (CD).

168 Mean annual air temperature (MAT) and mean annual precipitation (MAP) data



169 were downloaded from WorldClim version 2.1 (<https://www.worldclim.org>). These
170 datasets were generated by organizing, calculating, and spatially interpolating observed
171 data from global meteorological stations for the period 1970–2000.

172 Normalized difference vegetation index (NDVI) data were obtained from the
173 United States Geological Survey (USGS) (<http://modis.gsfc.nasa.gov/>). The datasets
174 underwent atmospheric, radiometric, and geometric correction, with a spatial resolution
175 of 1 km × 1 km for every 1-month interval over the period 2000–2015. The NDVI
176 product was calculated using the maximum value composite (MVC) method, which can
177 minimize the effects of aerosols and clouds (Stow et al., 2004).

178 The net primary productivity (NPP) and leaf area index (LAI) data were obtained
179 from the Global Land Surface Satellite (GLASS, V3.1), which is estimated from the
180 MODIS reflectance data using the general regression neural network (GRNN) method
181 (Liang et al., 2013). Data were at a 1 km resolution for 8 day periods between 2000 and
182 2015, and were downloaded from the National Earth System Science Data Center of
183 the National Science & Technology Infrastructure of China (<http://www.geodata.cn>).

184 The soil texture data, including sand, silt, and clay contents, were obtained from
185 the “SoilGrids250m database” (<http://www.isric.org>). The original 250 m spatial
186 resolution data were resampled to a 1 km resolution based on nearest neighbor
187 interpolation using ArcGIS 10.2 software (ESRI, Redlands, CA, USA). A digitized soil
188 taxonomy map was provided by the Harmonized World Soil Database version 1.2
189 (<http://www.fao.org/>), which combines existing national soil information worldwide (1
190 km resolution).

191 The land cover data used in this study were collected from the Land Cover Type
192 Climate Modeling Grid (CMG) product (MCD12C1) from 2010
193 (<https://lpdaac.usgs.gov>). The classification schemes in this study were based on the
194 global vegetation classification scheme of the International Geosphere Biosphere
195 Programme (IGBP). We reclassified the land cover types into five major categories:
196 forest, shrub, grassland, cropland, and desert.

197 **2.3 Model predictions**

198 In this study, three machine learning methods (random forest (RF), gradient



199 boosted regression tree (GBRT), and support vector machine (SVM)) were constructed
200 and validated using the SOCS in the upper 30 cm of soil profiles along with associated
201 variables.

202 With respect to the machine learning methods used, RF is used for classification,
203 regression, and other tasks. It is operated by constructing a large number of decision
204 trees during training, and outputs the class as the classification or regression patterns of
205 single trees (Tin Kam, 1998). The GBRT method is an iterative fitting algorithm
206 composed of multiple regression trees, and combines regression trees with a boosting
207 technique to improve predictive accuracy (Elith et al., 2008). The SVM regression
208 method uses kernel functions to construct an optimal hyperplane, which has a minimal
209 total deviation (Drake and Guisan, 2006). Combined with the remotely sensed data and
210 spatial interpolation data, RF, GBRT, and SVM regression were conducted to predict
211 the SOCS in the Third Pole region. The ‘randomForest’, ‘gbm’, and ‘e1071’ packages
212 in R were used to perform RF, GBRT, and SVM analyses.

213 The 15 input variables (H, S, TWI, TCA, RSP, CNB, CND, VD, NDVI, NPP, LAI,
214 MAP, MAT, sand, and silt) for the three regression models were selected because they
215 can reflect the effects of topography, climate, vegetation, and soil properties on regional
216 SOCSs. Moreover, these variables were significantly associated with the SOCS at a
217 depth interval of 0–30 cm ($P < 0.01$, Table S2), whereas other environmental factors
218 were eliminated due to their low correlation coefficients.

219 To generate the spatial distributions of SOCS in deep layers (below a depth of 100
220 cm), we established nonlinear extrapolation models (Fig. 3.a–b; Eqs. (2)–(4)) between
221 the SOCS in the upper 100 cm interval and the SOCS in the upper 200 cm interval using
222 the data from the 200 soil pits in grassland ($n = 151$) and desert ecosystems ($n = 49$,
223 Fig. A1). A third extrapolation model between the SOCS in the upper 200 cm interval
224 and the SOCS in the upper 300 cm interval in grassland ecosystems was established
225 using the data from 114 sites reported by Ding et al. (2016) (Fig 3.c; Eq. (4)).

$$226 \quad \ln SOCS_{0-200\text{cm}} = 0.9708 \times \ln SOCS_{0-100\text{cm}} + 0.3128 \quad (2)$$

$$227 \quad \ln SOCS_{0-200\text{cm}} = 0.8690 \times \ln SOCS_{0-100\text{cm}} + 0.7649 \quad (3)$$



$$\ln SOCS_{0-300cm} = 0.9521 \times \ln SOCS_{0-200cm} + 0.3296 \quad (4)$$

where $\ln SOCS_{0-100cm}$, $\ln SOCS_{0-200cm}$ and $\ln SOCS_{0-300cm}$ are the natural logarithms of the soil organic carbon stocks ($\text{kg} \cdot \text{m}^{-2}$) at the depth intervals of 0–100 cm, 0–200 cm, and 0–300 cm, respectively.

It is impossible to build extrapolation models directly to estimate deep SOC storage in forest, shrub, and cropland ecosystems, which lack deep soil pits below 100 cm. Therefore, according to the vertical distribution of the SOCS associated with different land cover types worldwide from Jobbagy and Jackson (2000), the extrapolation models shown in Eqs. (5)–(6) were established indirectly to estimate deep SOC storage (below a depth of 100 cm) in areas of these land cover types (Fig. S1). Correspondingly, Eq. (7) was established to estimate the deep SOC storage (below a depth of 200 cm) in desert ecosystems due to a lack of deep soil pits below 200 cm.

$$SOCS_{0-200cm} = (1 + \beta_{100-200cm}) \times SOCS_{0-100cm} \quad (5)$$

$$SOCS_{0-300cm} = (1 + \beta_{100-200cm} + \beta_{200-300cm}) \times SOCS_{0-100cm} \quad (6)$$

$$SOCS_{0-300cm} = SOCS_{0-200cm} + \beta_{200-300cm} \times SOCS_{0-100cm} \quad (7)$$

where $\beta_{100-200cm}$ and $\beta_{200-300cm}$ are proportion of $SOCS_{100-200cm}$ and $SOCS_{200-300cm}$ in $SOCS_{0-100cm}$, respectively.

The calculation of the SOC storage (Pg) for a region generally uses Eq. (8):

$$SOC_{storage} = \sum_{i=1}^n SOCS_i \times A \times 10^{-12} \quad (8)$$

where $SOCS_i$ is the SOCS ($\text{kg} \cdot \text{m}^{-2}$) at site i and A is the area (m^2) of each grid unit.

To test the predictive effects of the two machine learning methods, “leave-one-out” cross-validation was conducted. We used the R^2 value, the mean error (ME , Eq. (9)), and the root mean square error ($RMSE$, Eq. (10)) to evaluate the performance of the prediction models.

$$ME = \frac{1}{n} \sum_{i=1}^n [D(x_i) - D^*(x_i)] \quad (9)$$

$$RMSE = \sqrt{\frac{1}{n} \sum_{i=1}^n [D(x_i) - D^*(x_i)]^2} \quad (10)$$

where $D(x_i)$ is the measured SOCS, $D^*(x_i)$ is the predicted SOCS, and n is the number



255 of validation sites.

256 **3 Results**

257 **3.1 Performance of machine learning methods**

258 The results of the “leave-one-out” cross-validation showed that the RF model
259 exhibited a Pearson’s correlation coefficient of 0.81, which was higher than that of the
260 GBRT model (0.79) and SVM model (0.77). In addition, the *RMSE* of the RF model
261 ($3.01 \text{ kg}\cdot\text{m}^{-2}$) was lower than that of the GBRT model ($3.11 \text{ kg}\cdot\text{m}^{-2}$) and SVM model
262 ($3.21 \text{ kg}\cdot\text{m}^{-2}$) for the upper 30 cm of the soil profile. These results suggest that the RF
263 model provides a better tool for predicting the spatial distribution of SOCS in the Third
264 Pole region. Moreover, in order to further discuss the simulation accuracy of the RF
265 model in this study, “leave-one-out” cross-validations were conducted for depth
266 intervals of 0–50 cm and 0–100 cm. The results revealed high R^2 as well as low *RMSE*
267 and *ME* values (Fig. 6).

268 **3.2 Storage and spatial distribution of soil organic carbon**

269 Figure 7 shows a large spatial variability of the SOCS across the Third Pole region,
270 whereby an overall decreasing trend can be observed from the southeast towards the
271 northwest. The wetland area in the eastern region of the Third Pole (Ruoergai) had the
272 highest predicted SOCS for a depth interval of 0–300 cm ($> 32 \text{ kg}\cdot\text{m}^{-2}$), whereas the
273 northern region (Qiangtang Plateau and Qaidam Basin) had the lowest SOCS ($< 8 \text{ kg}\cdot\text{m}^{-2}$).
274 The estimated mean SOCS for the entire Third Pole region at depth intervals of 0–
275 30 cm, 0–50 cm, 1–100 cm, 0–200 cm, and 0–300 cm was $4.84 \text{ kg}\cdot\text{m}^{-2}$, $6.45 \text{ kg}\cdot\text{m}^{-2}$,
276 $8.51 \text{ kg}\cdot\text{m}^{-2}$, $11.57 \text{ kg}\cdot\text{m}^{-2}$, and $14.17 \text{ kg}\cdot\text{m}^{-2}$, respectively. Correspondingly, the total
277 estimated SOC storage was 15.79 Pg, 21.04 Pg, 27.75 Pg, 37.71 Pg, and 46.18 Pg at 0–
278 30 cm, 0–50 cm, 0–100 cm, 0–200 cm, and 0–300 cm, respectively (Table 2). In
279 addition, the SOCS decreased with increasing soil depth across the Third Pole region,
280 with 34.26% of the total SOC storage for a depth interval of 0–300 cm being contained
281 in the uppermost 30 cm, and only 17.89% in the 200–300 cm depth interval.

282 Compared with the area of seasonally frozen ground, the mean SOCS and total SOC
283 storage in the permafrost region were lower in each soil layer. The estimated amount of
284 SOC stored at a depth interval of 0–300 cm in the permafrost and seasonal frozen



285 ground zone were 21.69 Pg and 24.49 Pg, respectively, which accounted for 46.97%
286 and 53.03% of the total SOC pools, respectively.

287 The mean SOCS differed significantly among the various vegetation types ($P < 0.05$),
288 and were ranked as: forest > shrub > cropland > grassland > desert (Fig. 8). The
289 estimated SOC storage at a depth interval of 0–300 cm in forest, shrub, cropland,
290 grassland, and desert areas was 3.30 Pg, 0.85 Pg, 31.67 Pg, 9.77 Pg, and 0.59 Pg, thus
291 accounting for 7.15%, 1.84%, 68.58%, 21.57%, and 1.28% of the total, respectively.

292 According to the Harmonized World Soil Database, soils in the Third Pole region can
293 be divided into 21 main orders. Table 3 shows that the mean SOCS differed significantly
294 among various soil orders. The highest mean SOCS was for histosols ($39.45 \text{ kg}\cdot\text{m}^{-2}$),
295 which was ~3 times higher than that for leptosols ($14.17 \text{ kg}\cdot\text{m}^{-2}$), calcisols ($11.50 \text{ kg}\cdot\text{m}^{-2}$),
296 cambisols ($11.36 \text{ kg}\cdot\text{m}^{-2}$), lithosols ($12.91 \text{ kg}\cdot\text{m}^{-2}$), and regosols ($11.32 \text{ kg}\cdot\text{m}^{-2}$). The
297 mean SOCS values of chernozems, greyzems, gleysols, podzoluvisols, and luvisols
298 were all $> 20 \text{ kg}\cdot\text{m}^{-2}$, whereas those of arenosols, salt flats, and solonchaks were all $<$
299 $8 \text{ kg}\cdot\text{m}^{-2}$. Due to the differences in the mean SOCS values and distribution area, the
300 total SOC storage of each soil order also differed significantly. The total SOC storage
301 of leptosols was ~25.41 Pg for a depth interval of 0–300 cm, thus accounting for 55.02%
302 of the total SOC pool in the area of frozen ground on the QTP, while other soil orders
303 were $< 5 \text{ Pg}$.

304 **4 Discussion**

305 Due to the lack of systematic field observations, soil is still the part of the terrestrial
306 carbon cycle with the least amount of data, and the estimation of regional SOC pools
307 remains uncertain. Relatively few studies have estimated the SOC pool of the Third
308 Pole region. Most studies related to the Chinese part of the QTP (Tian et al., 2008; Wu
309 et al., 2008), or focused on the SOC storage of a certain vegetation type or certain area
310 (Wang et al., 2002). In addition, it is difficult to obtain data for deep soil horizons in the
311 Third Pole region due to complex terrain and harsh environment. Hence, most terrestrial
312 SOCS studies have focused on the shallow soil layer within 100 cm (Bai et al., 2010;
313 Fang et al., 1996; Yang et al., 2008), especially that of permafrost zones (Ding et al.,
314 2016; Mu et al., 2015; Wang et al., 2020; Zhao et al., 2018).



315 To date, few studies have, therefore, investigated the SOC storage and spatial patterns
316 in areas of seasonally frozen ground in the Third Pole region. Our study provides new
317 and more accurate data on SOC storage and spatial patterns for a depth interval of 0–3
318 m at a 1 km² scale over the Third Pole region, thus providing basic data for future
319 studies pertaining to Earth system modeling. We note that a lack of deep soil pits in
320 forest, shrub, and cropland ecosystems (Fig. S2) means some uncertainties in the
321 estimation of deep SOC pools remain; however, the collective area of these ecosystems
322 accounts for < 6% of the total area of the Third Pole region and may have a relatively
323 small influence on total SOC pools (Fig. A1). Regardless, there is a need for large-scale
324 soil surveys that include these areas in order to obtain more accurate information on the
325 SOC storage and distribution in the Third Pole region. Furthermore, regional SOC pools
326 are affected by many other factors, such as soil moisture (Wu et al., 2016) and grazing
327 activities (Zhou et al., 2017), which were not considered in our study due to lack of
328 high-resolution data with a high accuracy. Future work should consider the influence
329 of these factors on SOC at a regional scale to obtain more accurate datasets.

330 **5. Data availability**

331 The dataset of SOCS in the Third Pole region is available at the
332 <https://doi.org/10.5281/zenodo.4293454> (Wang et al., 2020).

333 **6. Conclusions**

334 This study simulated the spatial pattern of the SOCS over the Third Pole region, and
335 systematically estimated the SOC storage (46.18 Pg) at a depth interval of 0–3 m for
336 the first time. Our results demonstrated that combining multi-environmental factors
337 with machine learning techniques (RF, SVM, and GBRT) can offer an effective and
338 powerful modeling approach for mapping the spatial patterns of SOC. Furthermore, this
339 study provided datasets of SOCS and SOC storage for permafrost and seasonally frozen
340 ground, as well as for various vegetation/soil types at different soil depths (0–30 cm,
341 0–50 cm, 0–100 cm, 0–200 cm, and 0–300 cm) across the Third Pole region. These
342 datasets can be used to modify existing Earth system models and improve prediction
343 accuracy, and also serve as a reference for policymakers to formulate more effective
344 carbon budget management strategies.



345 **Author contributions**

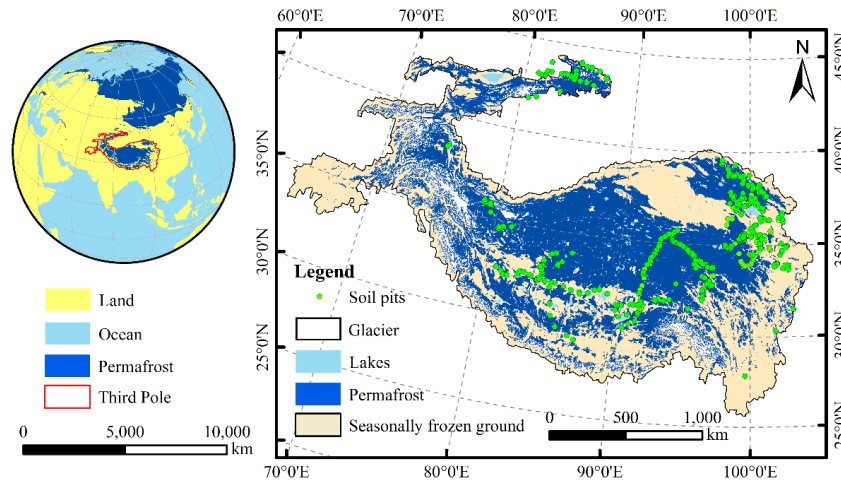
346 The study was completed with cooperation between all authors. Tonghua Wu and
347 Xiaodong Wu conceived the idea of mapping the spatial distribution of the SOC across
348 the Third Pole regions. Dong Wang conducted the data analyses and wrote the paper.
349 All authors discussed the simulation results and helped revise the paper.

350 **Competing interests**

351 The authors declare that they have no conflict of interest.

352 **Acknowledgements**

353 This work was financially supported by the State Key Laboratory of Cryospheric
354 Science (SKLCS-ZZ-2020), the National Natural Science Foundations of China
355 (41690142, 41721091, 41771076, 41961144021, 41671070), and the CAS "Light of
356 West China" Program.

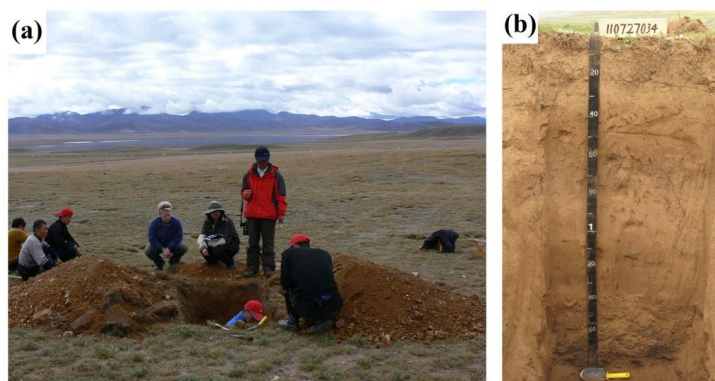


357

358 **Figure 1.** Distribution of soil pits in the Third Pole region (the frozen ground map is derived from

359

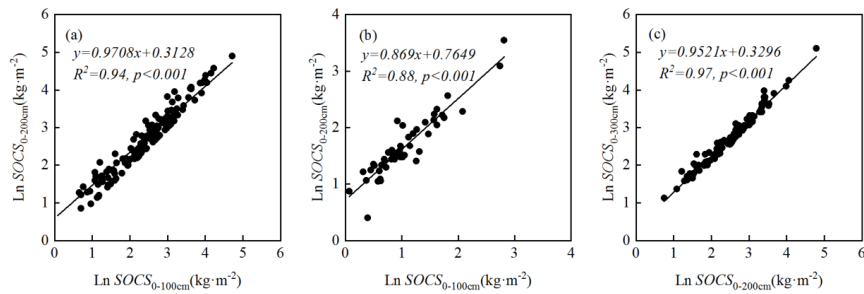
Obu et al., 2019).



360

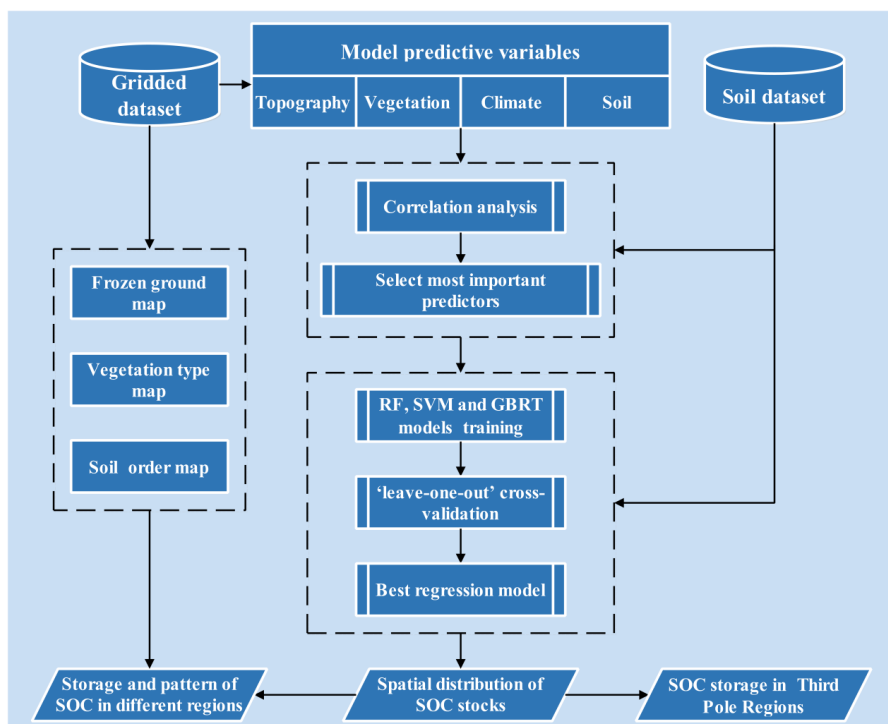
361

Figure 2. Field work photographs showing (a) soil sample collection, and (b) a soil profile.



362

363 **Figure 3.** Extrapolation function of the SOCS between soil depth intervals of (a) 0–100 cm and 0–
364 200 cm in grassland ecosystems, (b) 0–100 cm and 0–200 cm in desert ecosystems, and (c) 0–200
365 cm and 0–300 cm in grassland ecosystems.

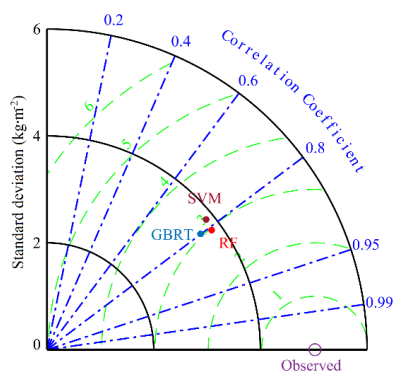


366

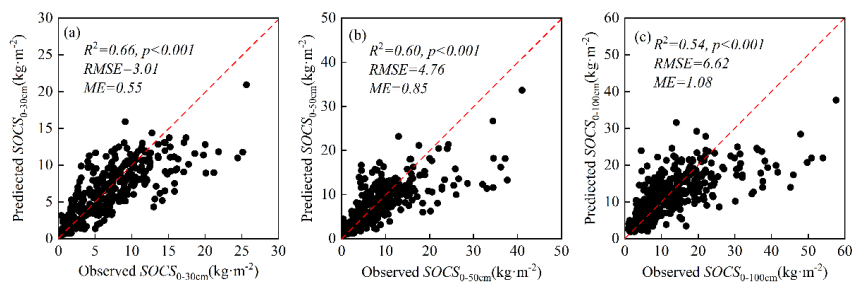
367

368

Figure 4. Workflow diagram for predicting SOCSS in this study. RF: random forest; SVM: support vector machine; GBRT: gradient boosted regression tree.



369
370 **Figure 5.** A Taylor diagram used to evaluate the model performance of random forest (RF),
371 support vector machine (SVM), and gradient boosting regression tree (GBRT) models, which
372 were used to predict the SOCS in the upper 30 cm of soil profiles across the Third Pole. The
373 contour centered on the observed indicates the root-mean-square error ($RMSE$, $\text{kg} \cdot \text{m}^{-2}$) between
374 the predicted value and observed value.

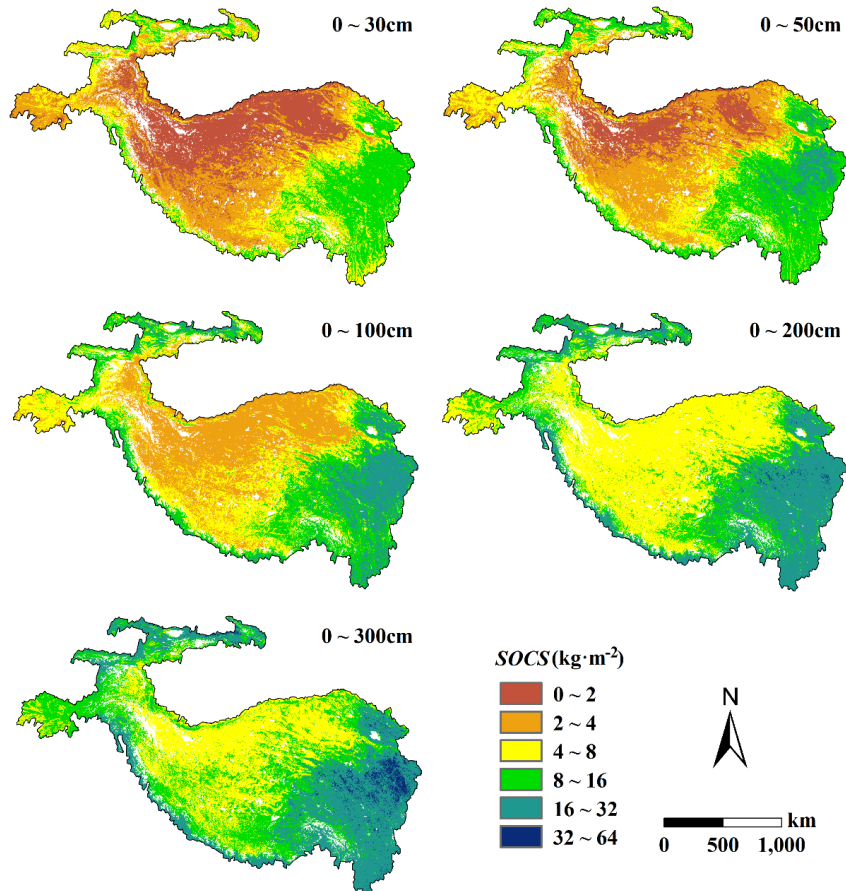


375

376 **Figure 6.** “Leave-one-out” cross-validation for the RF model used to predict the SOCS at (a) 0–30

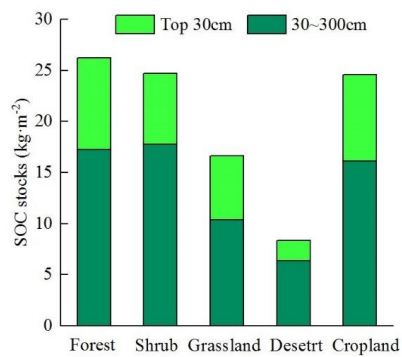
377

cm, (b) 0–50 cm, and (c) 0–100 cm depth intervals.



378

379 **Figure 7.** Spatial distribution of SOCS at different depth intervals over the Third Pole region.



380

381 **Figure 8.** Summary of the estimated SOC stocks of different vegetation types in the Third Pole.



382

Table 1 Summary of soil organic carbon datasets used in this study

Number of samples	Depth interval	Period	Method	Source
135	0–30 cm, 0–50, and 0–100 cm	2001–2005	Walkley-black method	Yang et al., 2010
30	Genetic horizon	2012–2013	Walkley-black method	Song et al., 2016
93	0–100 cm	2004–2014	Walkley-black method	Xu et al., 2019
113	0–200 cm and 0–300 cm	2013–2014	Walkley-black method	Ding et al., 2016
200	0–200 cm	2009–2013	Walkley-black method	Field-measured

383



384 **Table 2** Summary of the estimated mean SOC stocks and storages in permafrost and seasonally
 385 frozen ground of the Third Pole

Depth (cm)	SOC stock ($\text{kg}\cdot\text{m}^{-2}$)			SOC storage (Pg)		
	Permafrost	Seasonally frozen ground	Third Pole	Permafrost	Seasonally frozen ground	Third Pole
0–30	4.13	5.56	4.84	7.61	8.63	15.79
0–50	5.72	7.16	6.45	10.53	11.12	21.04
0–100	7.28	9.70	8.51	13.41	15.06	27.75
0–200	10.25	12.88	11.57	18.88	19.99	37.71
0–300	12.52	15.40	14.17	21.69	24.49	46.18

386



387 **Table 3** Summary of the estimated mean SOC stock and storage of different soil orders in the

388

Third Pole

Soil order	Area (10 ³ km ²)	SOC stock (kg·m ⁻²)			SOC storage (Pg)		
		0–30	0–100	0–300	0–30	0–100	0–300
		cm	cm	cm	cm	cm	cm
Leptosols	1793.53	4.84	8.51	14.17	8.68	15.26	25.41
Arenosols	60.59	1.78	3.88	7.87	0.11	0.24	0.48
Calcisols	89.44	3.59	6.64	11.50	0.32	0.59	1.03
Cambisols	313.14	3.62	6.58	11.36	1.13	2.06	3.56
Chernozems	78.31	8.47	14.45	22.47	0.66	1.13	1.76
Gypsisols	61.64	1.36	3.36	7.40	0.08	0.21	0.46
Greyzems	16.26	9.61	15.44	23.82	0.16	0.25	0.39
Gleysols	71.98	11.71	18.73	29.04	0.84	1.35	2.09
Kastanozems	34.59	6.07	10.39	16.47	0.21	0.36	0.57
Lithosols	367.94	4.34	7.57	12.91	1.60	2.79	4.75
Phaeozems	44.01	4.77	8.45	13.68	0.21	0.37	0.60
Luvvisols	156.35	9.37	15.71	25.04	1.46	2.46	3.92
Solonchaks	38.32	1.80	3.96	7.97	0.07	0.15	0.31
Salt flats	20.7	1.21	3.28	7.30	0.03	0.07	0.15
Histosols	3.62	13.33	27.36	39.45	0.05	0.10	0.14
Anthrosols	9.54	5.01	9.41	15.13	0.05	0.09	0.14
Fluvisols	8.97	3.06	5.78	10.19	0.03	0.05	0.09
Regosols	7.9	3.78	6.55	11.32	0.03	0.05	0.09
Podzols	7.28	1.92	3.76	8.01	0.01	0.03	0.06
Podzoluvissols	2.96	8.90	13.57	21.60	0.03	0.04	0.06
Rendzina	1.94	5.26	9.48	16.14	0.01	0.02	0.03

389 *Soil orders with an area of < 1 km² were not included.



390 **References**

- 391 Amundson, R.: The Carbon Budget in Soils, *Annual Review of Earth & Planetary Sciences*, 29,
392 535-562, <https://doi.org/10.1146/annurev.earth.29.1.535>, 2001.
- 393 Bai, J., Ouyang, H., Xiao, R., Gao, J., Gao, H., Cui, B., and Huang, L.: Spatial variability of
394 soil carbon, nitrogen, and phosphorus content and storage in an alpine wetland in the
395 Qinghai-Tibet Plateau, China, *Soil Research*, 48, 730-736, <https://doi.org/10.1071/SR09171>,
396 2010.
- 397 Chen, B. and Li, J.: Characteristics of Spatial and Temporal Variation of Seasonal and Short-
398 Term Frozen Soil in China in Recent 50 Years, *Chinese Journal of Atmospheric Sciences* (in
399 Chinese), 32, 432-443, 2008.
- 400 Ding, J., Li, F., Yang, G., Chen, L., Zhang, B., Liu, L., Fang, K., Qin, S., Chen, Y., Peng, Y., Ji,
401 C., He, H., Smith, P., and Yang, Y.: The permafrost carbon inventory on the Tibetan Plateau:
402 a new evaluation using deep sediment cores, *Global Change Biology*, 22, 2688-2701,
403 <https://doi.org/10.1111/gcb.13257>, 2016.
- 404 Ding, J., Wang, T., Piao, S., Smith, P., and Zhao, L.: The paleoclimatic footprint in the soil
405 carbon stock of the Tibetan permafrost region, *Nature Communications*, 10, 1-9,
406 <https://doi.org/10.1038/s41467-019-12214-5>, 2019.
- 407 Drake, J. M. and Guisan, R. A.: Modelling Ecological Niches with Support Vector Machines,
408 *Journal of Applied Ecology*, 43, 424-432, <https://doi.org/10.1111/j.1365-2664.2006.01141.x>,
409 2006.
- 410 Elith, J., Leathwick, J. R., and Hastie, T.: A working guide to boosted regression trees, *Journal*
411 *of Animal Ecology*, 77, 802-813, <https://doi.org/10.1111/j.1365-2656.2008.01390.x>, 2008.
- 412 Fan, J., Cao, Y., Yan, Y., Lu, X., Wang, X., Fan, J., Cao, Y., Yan, Y., Lu, X., and Wang, X.:
413 Freezing-thawing cycles effect on the water soluble organic carbon, nitrogen and microbial
414 biomass of alpine grassland soil in Northern Tibet, *African Journal of Microbiology Research*,
415 6, 562-567, <https://doi.org/10.5897/AJMR11.1218>, 2012.
- 416 Fang, J., Liu, G., and Xu, S.: Soil carbon pool in China and its global significance, *Journal of*
417 *Environmental Sciences*, 8, 249-254, <https://doi.org/10.3321/j.issn:1000-0585.2004.06.006>,
418 1996.
- 419 Hao, Y., Luo, X., Zhong, B., and Yang, A.: Methods of the National Vegetation Classification



420 based on Vegetation Partition, Remote Sensing Technology and Application, 32, 315-323,
421 <https://doi.org/10.2991/mmme-16.2016.60>, 2017.

422 Hugelius, G., Strauss, J., Zubrzycki, S., Harden, J. W., Schuur, E. A. G., Ping, C. L.,
423 Schirrmeister, L., Grosse, G., Michaelson, G. J., Koven, C. D., O'Donnell, J. A., Elberling,
424 B., Mishra, U., Camill, P., Yu, Z., Palmtag, J., and Kuhry, P.: Estimated stocks of circumpolar
425 permafrost carbon with quantified uncertainty ranges and identified data gaps,
426 Biogeosciences, 11, 6573-6593, <https://doi.org/10.5194/bg-11-6573-2014>, 2014.

427 Ji, Q., Yang, J., and Hongju, C.: Comprehensive analysis of the precipitation changes over the
428 Tibetan Plateau during 1961-2015, Journal of Glaciology and Geocryology, 40, 1090-1099,
429 <https://doi.org/10.7522/j.issn.1000-0240.2018.0415>, 2018.

430 Jiang, L., Chen, H., Zhu, Q., Yang, Y., Li, M., Peng, C., Zhu, D., and He, Y.: Assessment of
431 frozen ground organic carbon pool on the Qinghai-Tibet Plateau, Journal of Soils and
432 Sediments, 19, 128-139, <https://doi.org/10.1007/s11368-018-2006-3>, 2019.

433 Jobbagy, E. G. and Jackson, R. B.: The vertical distribution of soil organic carbon and its
434 relation to climate and vegetation, Ecological Applications, 10, 423-436,
435 <https://doi.org/10.2307/2641104>, 2000.

436 Koven, C. D., Ringeval, B., Friedlingstein, P., Ciais, P., Cadule, P., Khvorostyanov, D., Krinner,
437 G., and Tarnocai, C.: Permafrost carbon-climate feedbacks accelerate global warming,
438 Proceedings of the National Academy of Sciences, 2011.
439 <https://doi.org/10.1073/pnas.1103910108>, 2011.

440 Li, F., Zang, S., Liu, Y., Li, L., and Ni, H.: Effect of Freezing–Thawing Cycle on Soil Active
441 Organic Carbon Fractions and Enzyme Activities in the Wetland of Sanjiang Plain, Northeast
442 China, Wetlands, 40, 167-177, <https://doi.org/10.1007/s13157-019-01164-9>, 2020.

443 Liang, S., Zhao, X., Liu, S., Yuan, W., Cheng, X., Xiao, Z., Zhang, X., Liu, Q., Cheng, J., Tang,
444 H., Qu, Y., Bo, Y., Qu, Y., Ren, H., Yu, K., and Townshend, J.: A long-term Global Land
445 Surface Satellite (GLASS) dataset for environmental studies, International Journal of Digital
446 Earth, 6, 5-33, <https://doi.org/10.1080/17538947.2013.805262>, 2013.

447 Lombardozzi, D. L., Bonan, G. B., Smith, N. G., Dukes, J. S., and Fisher, R. A.: Temperature
448 acclimation of photosynthesis and respiration: A key uncertainty in the carbon cycle–climate
449 feedback, Geophysical Research Letters, 42, 8624-8631,



- 450 <https://doi.org/10.1002/2015GL065934>, 2016.
- 451 McGuire, A. D., Lawrence, D. M., Koven, C., Clein, J. S., Burke, E., Chen, G., Jafarov, E.,
452 Macdougall, A. H., Marchenko, S., Nicolsky, D., Peng, S., Rinke, A., Ciais, P., Gouttevin, I.,
453 Hayes, D. J., Ji, D., Krinner, G., Moore, J. C., Romanovsky, V., Schädel, C., Schaefer, K.,
454 Schuur, E. A. G., and Zhuang, Q.: Dependence of the evolution of carbon dynamics in the
455 northern permafrost region on the trajectory of climate change, *Proceedings of the National*
456 *Academy of Sciences*, 115, 3882-3887, <https://doi.org/10.1073/pnas.1719903115>, 2018.
- 457 Mu, C., Shang, J., Zhang, T., Fan, C., Wang, S., Peng, X., Zhong, W., Zhang, F., Mu, M., and
458 Jia, L.: Acceleration of thaw slump during 1997–2017 in the Qilian Mountains of the northern
459 Qinghai-Tibetan plateau, *Landslides*, 17, 1051-1062, [https://doi.org/10.1007/s10346-020-](https://doi.org/10.1007/s10346-020-01344-3)
460 [01344-3](https://doi.org/10.1007/s10346-020-01344-3), 2020.
- 461 Mu, C., Zhang, T., Wu, Q., Peng, X., Cao, B., Zhang, X., Cao, B., and Cheng, G.: Editorial:
462 Organic carbon pools in permafrost regions on the Qinghai–Xizang (Tibetan) Plateau, 9, 479-
463 486, <https://doi.org/10.5194/tc-9-479-2015>, 2015.
- 464 Obu, J., Westermann, S., Bartsch, A., Berdnikov, N., Christiansen, H. H., Dashtseren, A.,
465 Delaloye, R., Elberling, B., Etzelmüller, B., Kholodov, A., Khomutov, A., Kääb, A., Leibman,
466 M. O., Lewkowicz, A. G., Panda, S. K., Romanovsky, V., Way, R. G., Westergaard-Nielsen,
467 A., Wu, T., Yamkhin, J., and Zou, D.: Northern Hemisphere permafrost map based on TTOP
468 modelling for 2000–2016 at 1 km² scale, *Earth-Science Reviews*, 193, 299-316,
469 <https://doi.org/10.1016/j.earscirev.2019.04.023>, 2019.
- 470 Ping, C. L., Jastrow, J. D., Jorgenson, M. T., Michaelson, G. J., and Shur, Y. L.: Permafrost soils
471 and carbon cycling, *Soil*, 1, 147-171, <https://doi.org/10.5194/soil-1-147-2015>, 2015.
- 472 Qin, D., Ding, Y., Su, J., Ren, J., Wang, S., Wu, R., Yang, X., Wang, S., Liu, S., Dong, G., Lu,
473 Q., Huang, Z., Du, B., and Luo, Y.: Assessment of Climate and Environment Changes in
474 China (I): Climate and environment change in China and their projection *Climate Change*
475 *Research, Advances In Climate Change Research*, 01, 4-9,
476 <https://doi.org/10.3969/j.issn.1673-1719.2005.01.002>, 2005.
- 477 Qin, Y. H., Wu, T. H., Zhao, L., Wu, X. D., Li, R., Xie, C. W., Pang, Q. Q., Hu, G. J., Qiao, Y.
478 P., Zhao, G. H., Liu, G. Y., Zhu, X. F., and Hao, J. M.: Numerical Modeling of the Active
479 Layer Thickness and Permafrost Thermal State Across Qinghai-Tibetan Plateau, *Journal of*



- 480 Geophysical Research-Atmospheres, 122, 11604-11620,
481 <https://doi.org/10.1002/2017jd026858>, 2017.
- 482 Ran, Y., Li, X., and Cheng, G.: Climate warming has led to the degradation of permafrost
483 stability in the past half century over the Qinghai-Tibet Plateau. Copernicus GmbH,
484 <https://doi.org/10.5194/tc-2017-120>, 2017.
- 485 Schuur, E. A. G., McGuire, A. D., Schädel, C., Grosse, G., Harden, J. W., Hayes, D. J., Hugelius,
486 G., Koven, C. D., Kuhry, P., Lawrence, D. M., Natali, S. M., Olefeldt, D., Romanovsky, V.
487 E., Schaefer, K., Turetsky, M. R., Treat, C. C., and Vonk, J. E.: Climate change and the
488 permafrost carbon feedback, *Nature*, 520, 171-179, <https://doi.org/10.1038/nature14338>,
489 2015.
- 490 Song, X. D., Brus, D. J., Liu, F., Li, D.-C., Zhao, Y. G., Yang, J. L., and Zhang, G. L.: Mapping
491 soil organic carbon content by geographically weighted regression: A case study in the Heihe
492 River Basin, China, *Geoderma*, 261, 11-22, <https://doi.org/10.1016/j.geoderma.2015.06.024>,
493 2016.
- 494 Stocker, T. F., Qin, D., Plattner, G. K., Tignor, M., Allen, S. K., Boschung, J., Nauels, A., Xia,
495 Y., Bex, B., and Midgley, B. M.: IPCC, 2013: Climate Change 2013: The Physical Science
496 Basis. Contribution of Working Group I to the Fifth Assessment Report of the
497 Intergovernmental Panel on Climate Change, *Computational Geometry*, 18, 95-123, 2013.
- 498 Stow, D. A., Hope, A., McGuire, D., Verbyla, D., Gamon, J., Huemmrich, F., Houston, S.,
499 Racine, C., Sturm, M., Tape, K., Hinzman, L., Yoshikawa, K., Tweedie, C., Noyle, B.,
500 Silapaswan, C., Douglas, D., Griffith, B., Jia, G., Epstein, H., Walker, D., Daeschner, S.,
501 Petersen, A., Zhou, L., and Myneni, R.: Remote sensing of vegetation and land-cover change
502 in Arctic Tundra Ecosystems, *Remote Sensing of Environment*, 89, 281-308,
503 <https://doi.org/10.1016/j.rse.2003.10.018>, 2004.
- 504 Tian, Y., Ouyang, H., Xu, X., Song, M., and Zhou, C.: Distribution characteristics of soil
505 organic carbon storage and density on the Qinghai-Tibet Plateau, *Acta Pedologica Sinica*, 45,
506 933-942, 2008.
- 507 Tin Kam, H.: Random subspace method for constructing decision forests, *IEEE Transactions*
508 *on Pattern Analysis and Machine Intelligence*, 20, 832-844,
509 <https://doi.org/10.1109/34.709601>, 1998.



- 510 Turetsky, M. R., Abbott, B. W., Jones, M. C., Walter Anthony, K., Olefeldt, D., Schuur, E. A.
511 G., Koven, C., McGuire, A. D., Grosse, G., Kuhry, P., Hugelius, G., Lawrence, D. M., Gibson,
512 C., and Sannel, A. B. K.: Permafrost collapse is accelerating carbon release, *Nature*, 569, 32-
513 34, <https://doi.org/10.1038/d41586-019-01313-4>, 2019.
- 514 Wang, G., Qian, J., Cheng, G., and Lai, Y.: Soil organic carbon pool of grassland soils on the
515 Qinghai-Tibetan Plateau and its global implication, *Science of the Total Environment*, 291,
516 207-217, [https://doi.org/10.1016/S0048-9697\(01\)01100-7](https://doi.org/10.1016/S0048-9697(01)01100-7), 2002.
- 517 Wang, T. H., Yang, D. W., Yang, Y. T., Piao, S. L., Li, X., Cheng, G. D., and Fu, B. J.: Permafrost
518 thawing puts the frozen carbon at risk over the Tibetan Plateau, *Science Advances*, 6,
519 <https://doi.org/10.1126/sciadv.aaz3513>, 2020.
- 520 Wu, Q., Zhang, T., and Liu, Y.: Thermal state of the active layer and permafrost along the
521 Qinghai-Xizang (Tibet) Railway from 2006 to 2010, *The Cryosphere*, 6, 607-612,
522 <https://doi.org/10.5194/tc-6-607-2012>, 2012.
- 523 Wu, X., Zhao, L., Fang, H., Zhao, Y., Smoak, J. M., Pang, Q., and Ding, Y.: Environmental
524 controls on soil organic carbon and nitrogen stocks in the high-altitude arid western Qinghai-
525 Tibetan Plateau permafrost region, *Journal of Geophysical Research Biogeosciences*, 121,
526 176-187, <https://doi.org/10.1002/2015JG003138>, 2016.
- 527 Wu, Y., Liu, G., Fu, B., and Guo, Y.: Study on the vertical distribution of soil organic carbon
528 density in the Tibetan Plateau, *Acta Scientiae Circumstantiae*, 28, 362-367,
529 <https://doi.org/10.3724/SP.J.1148.2008.00259>, 2008.
- 530 Xu, L., Yu, G., and He, N.: Increased soil organic carbon storage in Chinese terrestrial
531 ecosystems from the 1980s to the 2010s, *Journal of Geographical Sciences*, 29, 49-66,
532 <https://doi.org/10.1007/s11442-019-1583-4>, 2019.
- 533 Yang, Y., Fang, J., Ma, W., Smith, P., Mohammad, A., Wang, S., and Wang, W.: Soil carbon
534 stock and its changes in northern China's grasslands from 1980s to 2000s, *Global Change
535 Biology*, 16, 3036-3047, <https://doi.org/10.1111/j.1365-2486.2009.02123.x>, 2010.
- 536 Yang, Y., Fang, J., Tang, Y., Ji, C., Zheng, C., He, J., and Zhu, B.: Storage, patterns and controls
537 of soil organic carbon in the Tibetan grasslands, *Global Change Biology*, 14, 1592-1599,
538 <https://doi.org/10.1111/j.1365-2486.2008.01591.x>, 2008.
- 539 Yao, T., Thompson, L. G., Mosbrugger, V., Zhang, F., Ma, Y., Luo, T., Xu, B., Yang, X., Joswiak,



540 D. R., Wang, W., Joswiak, M. E., Devkota, L. P., Tayal, S., Jilani, R., and Fayziev, R.: Third
541 Pole Environment (TPE), *Environmental Development*, 3, 52-64,
542 <https://doi.org/10.1016/j.envdev.2012.04.002>, 2012.

543 Zeng, Y., Feng, Z., Cao, G., and Xu, L.: The Soil Organic Carbon Storage and Its Spatial
544 Distribution of Alpine Grassland in the Source Region of the Yellow River, *Acta Geographica*
545 *Sinica*, 59, 497-504, <https://doi.org/10.1007/BF02873091>, 2004.

546 Zhao, L., Wu, X., Wang, Z., Sheng, Y., Fang, H., Zhao, Y., Hu, G., Li, W., Pang, Q., Shi, J., Mo,
547 B., Wang, Q., Ruan, X., Li, X., and Ding, Y.: Soil organic carbon and total nitrogen pools in
548 permafrost zones of the Qinghai-Tibetan Plateau, *Scientific Reports*, 8,
549 <https://doi.org/10.1038/s41598-018-22024-2>, 2018.

550 Zhou, G., Zhou, X., He, Y., Shao, J., Hu, Z., Liu, R., Zhou, H., and Hosseinibai, S.: Grazing
551 intensity significantly affects belowground carbon and nitrogen cycling in grassland
552 ecosystems: a meta-analysis, *Global Change Biology*, 23, <https://doi.org/1167-1179>,
553 10.1111/gcb.13431, 2017.

554